The Astrophysical Journal, 892:64 (10pp), 2020 March 20 https://doi.org/10.3847/1538-4357/ab792a

The Origin of Binary Black Hole Mergers

Zoe Piran and Tsvi Piran
Racah Institute of Physics, The Hebrew University, Jerusalem 91904, Israel
Received 2019 December 25; revised 2020 February 19; accepted 2020 February 20; published 2020 March 30

Abstract

Recently Venumadhav et al. proposed a new pipeline to analyze LIGO–Virgo Collaboration's O1–O2 data, and discovered eight new binary black hole (BBH) mergers, including one with a high effective spin, $\chi_{\rm eff}$. This discovery helps to clarify the origin of the observed BBHs and the dynamical capture versus field binaries debate. Using a tide-wind model that characterizes the late phases of binary evolution and captures the essence of field binary spin evolution, we show that the observed $\chi_{\rm eff}$ distribution favors this model over capture. However, given the current limited sample size, capture scenarios (isotropic models) cannot be ruled out. Observations of roughly 100 merges will enable us to distinguish between the different formation scenarios. However, if as expected, both formation channels operate, it may be difficult to resolve their exact fraction.

Unified Astronomy Thesaurus concepts: Gravitational waves (678); Gravitational wave sources (677)

1. Introduction

The Ligo–Virgo Collaboration (LVC) discovery (Abbott et al. 2016, 2019a, 2019b) of merging binary black holes (BBH) immediately posed a puzzle—what is the origin of these binaries? The numerous models that have been suggested can be divided to two main groups: "field evolution" models and dynamical capture models. In the former, the BBHs arose from binary massive stellar progenitor (e.g., Phinney 1991; Tutukov & Yungelson 1993; Belczynski et al. 2016; Mandel & de Mink 2016; Marchant et al. 2016; Belczynski et al. 2017; O'Shaughnessy et al. 2017; Stevenson et al. 2017; Qin et al. 2018; Postnov & Mitichkin 2019; Bavera et al. 2020). In the latter, each one of the black holes formed on its own, and the binary was assembled via a dynamical capture. These latter scenarios are further divided into two physically different subgroups. In the first scenario, the BBHs are primordial (e.g., Ioka et al. 1998; Rubin et al. 2001; Bird et al. 2016; Blinnikov et al. 2016; Kashlinsky 2016; Sasaki et al. 2016). In the second scenario, they formed from regular massive stars in various dense stellar environments in which the interaction with other stars led to the formation of the binary (Sigurdsson & Hernquist 1993; Portegies Zwart & McMillan 2000; Miller & Lauburg 2009; O'Leary et al. 2009; Kocsis & Levin 2012; Antonini & Rasio 2016; Rodriguez et al. 2016, 2018; O'Leary et al. 2016; Bartos et al. 2017; Stone et al. 2017; Fragione & Kocsis 2018; Hoang et al. 2018; McKernan et al. 2018; Fragione et al. 2019; Secunda et al. 2019).

It has been long realized (Mandel & O'Shaughnessy 2010) that among the different parameters of a merging black hole binary, which can be easily recovered from the GW data,[1] the effective spin, $-1 \leqslant \chi_{\rm eff} \leqslant 1$ (the normalized component of the sum of the two black holes spins projected in the direction of the orbital spin), is the most informative parameter for studying the BBH origin (see also Blinnikov et al. 2016; Kushnir et al. 2016; Hotokezaka & Piran 2017). The normalized spin of each black hole is defined as $\chi \equiv c\boldsymbol{S}\cdot\hat{\boldsymbol{L}}/Gm^2$, where m is the black hole's mass, $\boldsymbol{S}$ its spin vector, $\hat{\boldsymbol{L}}$ is the direction of the orbital spin, and c and G are the speed of light and Newton's constant, respectively. The binary's effective spin is $\chi_{\rm eff} \equiv (\chi_{\rm BH,1} + q\chi_{\rm BH,2})/(1+q)$ with $q \equiv m_2/m_1$.

Capture scenarios do not provide a physical mechanism that links the directions of spins of the individual black holes to the orbital angular momentum. The former depends on the evolution of the individual black holes' progenitors, while the latter depends on their relative motion and the capture dynamics. This results in what we denote as *"isotropic"* $\chi_{\rm eff}$ distribution (Rodriguez et al. 2016). In this case, the spins are randomly oriented relative to each other and to the orbital spin. Thus, we expect both positive and negative $\chi_{\rm eff}$ values. As triple alignments are rare, we do not expect large $|\chi_{\rm eff}|$ values, and in any case we expect equal number of positive and negative ones.[2] In the following, we will consider (following Farr et al. 2017), three isotropic distributions: low, flat, and high, according to the distribution of the spins' magnitudes (see Figure 2).

On the other hand, various processes during the evolution of "field binaries" align the stellar spins with the orbit. Among those are (i) the binary formation process, if the progenitor stars formed from a rotating cloud; (ii) mass transfer that spins the recipient along the direction of the orbital motion; (iii) tidal locking at various stages, especially at the late phases of the binary. Some mechanisms, in particular winds, reduce the progenitors spins. Others, such as kicks during the collapse (Mandel 2016; Tauris et al. 2017; Wysocki et al. 2018), randomize it, changing its direction, and possibly magnitude.[3] However, no known mechanism preferably rotates the stellar spins into a direction opposite to the orbital angular momentum. Hence, we expect a positive correlation between individual spins and the orbit's angular momentum leading to a preference of positive $\chi_{\rm eff}$ values over what is expected in an isotropic distribution (see Figure 4).

Numerous attempts to model the expected distributions of BBH mergers parameters (masses, mass ratios, spins, etc.) within the "field binaries" scenario have been carried out using

[1] Spin measurements of individual BHs that might be available in the future may help to clarify this question.

[2] Note that selection bias that depend on $\chi_{\rm eff}$ (Campanelli et al. 2006a; Roulet & Zaldarriaga 2019) may lead to excess of positive $\chi_{\rm eff}$ events, but those can be taken into account only when sufficient data is available.

[3] A change in the magnitude may arise if the kick is not give at the CM of the collapsing star.

a detailed population synthesis approach (see, e.g., Belczynski et al. 2016, 2017; Wiktorowicz et al. 2019; Bavera et al. 2020). These models follow all stages of stellar evolution from birth to death using the best current understanding of each phase, and construct expected distributions of all observed parameters. However, various unknown factors concerning critical phases during the binary evolution (see e.g., Ivanova et al. 2013 for a review concerning the common envelope phase) exist. Instead, following (Kushnir et al. 2016; Hotokezaka & Piran 2017; Piran & Hotokezaka 2018), we consider here a minimal model that identifies tidal locking and winds that operate at the latest stages of the stellar evolution as the dominant mechanisms that determine the black hole's spins and the system's $\chi_{\rm eff}$. We take into account all earlier effects by varying the initial conditions of this final stage. The virtue of this model is its simplicity. It includes only two free parameters which are sufficient to capture the essence of the observed $\chi_{\rm eff}$ distribution. The simplicity of the model implies that it cannot capture some of the rich features of this last phase (see Qin et al. 2018; Bavera et al. 2020, for a detailed discussion). These are particularly important concerning the impact of winds that we discuss below. However, this approach is justified given the relatively small size of the current observed data set that provides us limited statistical knowledge about the population.

This model (as we elaborate in Section 3 and Appendix A) considers only the last phase of the binary after the primary star has already collapsed to a black hole and it exerts a tidal force on its companion. At the same time, strong winds reduce the companion's spin. The competition between tides and winds determines the final progenitor's spin.[4] To account for the uncertainty in the earlier phases of the stellar evolution, we consider two drastically different initial conditions at the beginning of this phase: the secondary star is either nonrotating or it is fully synchronized with the orbital motion. As for the primary, we consider it to either follow a similar evolution as the secondary (namely spins and tides) or to be randomly oriented.

LVC's O1–O2 events distribution is approximately symmetric around 0 with a rather low $\chi_{\rm eff}$ values. Such a distribution favors a low-isotropic model (Farr et al. 2017; Wysocki et al. 2018). However, this sample did not provide enough events to rule out "field binary" scenarios (Piran & Hotokezaka 2018; Wysocki et al. 2018). The recent reanalysis of LVC's O1–O2 data recovered the 10 BBH mergers detected by LVC and revealed eight new events (Venumadhav et al. 2019a, 2019b; Zackay et al. 2019a, 2019b). We denote the combined set of observation as the LVC–IAS data set. Here, we consider the question of whether the newly identified mergers clarify the origin of these BBHs.

This work extends the analysis carried out by Piran & Hotokezaka (2018) for the LVC data to the larger LVC–IAS data set. In addition to a modified "field binary" model, we use a novel way to account for errors in the estimated $\chi_{\rm eff}$ values, and we evaluate the quality of the fits using the Anderson–Darling statistic. The LVC–IAS data set is still rather small, thus one cannot expect that it will conclusively rule out or confirm any one of the models. Furthermore, it is possible that some BBH merges form via field evolution while others are captured. Hence, we also ask how many mergers should be detected to enable us to distinguish between "isotropic" models and "field binary" models, and how many will be needed to distinguish between a pure "isotropic" or "field binary" model and a mixed one.

We describe the data sets in Section 2. We briefly discuss the models in Section 3 (leaving some details to a more technical in Appendix A) and describe the data analysis in Section 4. The results are presented in 5, discussing first the results concerning the current data Section 5.1, and then in Section 5.2 we explore the question how many events are needed to distinguish between different models. We summarize our findings in Section 6

2. The Data

The LVC analysis of the O1–O2 runs revealed ten BBH mergers (Abbott et al. 2019b). Recently, Venumadhav et al. (2019b) proposed a novel pipeline for the analysis of GW data. Estimated parameters of mergers identified by both pipelines are within the errors of each other (see Table 1 and Figure 1). However, the new reanalysis of the O1 (Zackay et al. 2019b) and O2 data (Venumadhav et al. 2019a; Zackay et al. 2019a) revealed eight new BBH mergers.

In the following analysis, we neglect possible mass/spin correlations. We evaluate the models over a fixed mass and compare them with the unweighted[5] observed distribution. This is natural in the isotropic scenario and valid for field binary scenarios if tidal locking and winds operate in the same manner across the progenitors mass range. Furthermore, given the small sample size, such an assumption is essential. For the same reason, we neglect (see, e.g., Abbott et al. 2019a) bias that may arise from the dependence of the GW horizon on the spin (Campanelli et al. 2006b; Roulet & Zaldarriaga 2019).

3. The Models.

3.1. Isotropic Models

The $\chi_{\rm eff}$ distribution is given by a weighted sum of two randomly oriented (isotropic) normalized spin vectors $\boldsymbol{s}_i$:

$$\chi_{\rm eff-iso} = \frac{\boldsymbol{s}_1 \cdot \hat{\boldsymbol{L}} + q\boldsymbol{s}_2 \cdot \hat{\boldsymbol{L}}}{1+q}. \quad (1)$$

Following Farr et al. (2017), we consider three distributions defined by the distribution of $|\boldsymbol{s}_i|$: flat or dominated by either low or high spins. The probability for a given $\boldsymbol{s}$ value is

$$p(|\boldsymbol{s}_i|) = \begin{cases} 2(1-|\boldsymbol{s}_i|) & \text{low;} \\ 1 & \text{flat;} \\ 2|\boldsymbol{s}_i| & \text{high.} \end{cases} \quad (2)$$

We use $q = 1$ (varying q has a minor effect; see Figure 9 in Appendix B).

3.2. Field Binaries

Given the complexity of binary evolution (see e.g., Qin et al. 2018; Bavera et al. 2020), we consider here a minimal model (Kushnir et al. 2016; Hotokezaka & Piran 2017; Piran & Hotokezaka 2018) that captures the critical ingredients during the last phase of the binary: the interplay between tidal locking, which increases and aligns the spin; and winds, which diminish it. We assume that the two processes (tidal locking and winds)

[4] As we explain later, we expect that natal kicks at the BH formation are unimportant.

[5] With respect to the mass.

Table 1
Parameters of the BBH Mergers Detected During LVC's O1 and O2 by LVC (Left Columns; Abbott et al. 2019b) and IAS (Right Columns; Venumadhav et al. 2019a; Zackay et al. 2019a)

Event	$m_1/M_\odot$		$m_2/M_\odot$		$\chi_{\rm eff}$		$p_{\rm astro}$
	LVC	IAS	LVC	IAS	LVC	IAS	IAS
GW150914	$35.6^{+4.8}_{-3.0}$	$35.9^{+4.47}_{-4.45}$	$30.6^{+3.0}_{-4.4}$	$29.6^{+3.5}_{-3.6}$	$-0.01^{+0.12}_{-0.13}$	$-0.05^{+0.11}_{-0.11}$	*
GW151012	$23.3^{+14.0}_{-5.5}$	$27.3^{+12.03}_{-11.89}$	$13.6^{+4.1}_{-4.8}$	$12.11^{+4.25}_{-4.2}$	$0.04^{+0.28}_{-0.19}$	$0.05^{+0.23}_{-0.23}$	>0.99
GW151226	$13.7^{+8.8}_{-3.2}$	$16.4^{+7.53}_{-7.5}$	$7.7^{+2.2}_{-2.6}$	$7.53^{+2.45}_{-2.47}$	$0.18^{+0.20}_{-0.12}$	$0.27^{+0.19}_{-0.19}$	*
GW170104	$31.0^{+7.2}_{-5.6}$	$30.17^{+5.95}_{-5.96}$	$20.1^{+4.9}_{-4.5}$	$19.6^{+3.89}_{-3.85}$	$-0.04^{+0.17}_{-0.20}$	$-0.09^{+0.16}_{-0.16}$	>0.99
GW170608	$10.9^{+5.3}_{-1.7}$	$17.4^{+11.43}_{-11.45}$	$7.6^{+1.3}_{-2.1}$	$5.8^{+2.66}_{-2.66}$	$0.03^{+0.19}_{-0.07}$	$0.25^{+0.3}_{-0.31}$	>0.99
GW170729	$50.6^{+16.6}_{-10.2}$	$50.3^{+12.42}_{-11.5}$	$34.3^{+9.1}_{-10.1}$	$34.6^{+9.05}_{-9.03}$	$0.36^{+0.21}_{-0.25}$	$0.43^{+0.21}_{-0.21}$	>0.99
GW170809	$35.2^{+8.3}_{-6.0}$	$36.1^{+7.8}_{-7.76}$	$23.8^{+5.2}_{-5.1}$	$23.6^{+4.95}_{-4.94}$	$0.07^{+0.16}_{-0.16}$	$0.08^{+0.19}_{-0.19}$	>0.99
GW170814	$30.7^{+5.7}_{-3.0}$	$31.0^{+4.53}_{-4.53}$	$25.3^{+2.9}_{-4.1}$	$24.98^{+3.29}_{-3.29}$	$0.07^{+0.12}_{-0.11}$	$0.05^{+0.11}_{-0.11}$	>0.99
GW170818	$35.5^{+7.5}_{-4.7}$	$35.4^{+5.92}_{-5.91}$	$26.8^{+4.3}_{-5.2}$	$26.87^{+4.59}_{-4.6}$	$-0.09^{+0.18}_{-0.21}$	$0.05^{+0.2}_{-0.2}$	>0.99
GW170823	$39.6^{+10.0}_{-6.6}$	$39.5^{+7.34}_{-7.43}$	$29.4^{+6.3}_{-7.1}$	$28.5^{+5.91}_{-5.91}$	$0.08^{+0.20}_{-0.22}$	$0.09^{+0.22}_{-0.22}$	>0.99
GW170121	⋯	$31.8^{+6.56}_{-6.58}$	⋯	$23.9^{+5.07}_{-5.05}$	⋯	$-0.3^{+0.29}_{-0.29}$	>0.99
GW170727	⋯	$40.1^{+8.34}_{-8.35}$	⋯	$29.1^{+6.6}_{-6.63}$	⋯	$-0.09^{+0.32}_{-0.33}$	0.98
GW170304	⋯	$42.9^{+9.79}_{-9.73}$	⋯	$31.6^{+7.5}_{-7.5}$	⋯	$0.19^{+0.31}_{-0.31}$	0.985
GW170817A	⋯	56^{+16}_{-10}	⋯	40^{+10}_{-11}	⋯	$0.5^{+0.2}_{-0.2}$	0.86
GW170425	⋯	$46.7^{+14.9}_{-14.92}$	⋯	$29.9^{+9.87}_{-9.91}$	⋯	$0.05^{+0.42}_{-0.42}$	0.77
GW151216	⋯	$32.3^{+9.7}_{-9.7}$	⋯	$20.47^{+5.76}_{-5.76}$	⋯	$0.8^{+0.18}_{-0.18}$	0.71
GW170202	⋯	$29.87^{+11.46}_{-11.45}$	⋯	$14.32^{+4.48}_{-4.48}$	⋯	$-0.16^{+0.34}_{-0.34}$	0.68
GW170403	⋯	$45.5^{+10.25}_{-10.25}$	⋯	$32.7^{+8.29}_{-8.25}$	⋯	$-0.63^{+0.39}_{-0.38}$	0.56

Note. The parameters are median values with 90% credible intervals.

are decoupled, and we neglect the possible interplay between the two, due to the fact that winds increase the orbital separation and this weakens the tidal force.

To account for the uncertainty in earlier phases of the evolution, we consider different initial conditions for the beginning of this last phase. We briefly outline here the essential ingredients, focusing in particular on revisions that we have introduced to the model used by Piran & Hotokezaka 2018). We consider Wolf–Rayet progenitors, as those are massive enough and have small enough radii allowing the binaries to merge within a Hubble time. However, the considerations are not limited to those and would be relevant to final stages of most field binaries, provided that their radii are small enough to fit within an orbit that can merge in a Hubble time. Numerical factors concerning the stellar model that we use in Equations (3)–(5) below may be different in such cases but the basic result holds.

Coalescence. We assume that at the time that the second BH forms the orbit is circular (see, e.g., Hotokezaka & Piran 2017; Mirabel 2017) with a radius a. The corresponding coalescence time is

$$t_c \approx 10\mathrm{Gyr}\left(\frac{2q^2}{1+q}\right)\left(\frac{a}{44R_\odot}\right)^4\left(\frac{m_2}{30M_\odot}\right)^{-3}. \quad (3)$$

We use this equation to express the orbital separation in terms of t_c. Consequently, the t_c distribution, discussed below, determines the orbital separation distribution and vice versa.

Synchronization. The synchronization of the spin of a massive star due to the tidal force exerted by the companion has been studied in different contexts by numerous authors (Brown et al. 2000; Izzard et al. 2004; Petrovic et al. 2005; Cantiello et al. 2007; van den Heuvel 2007; Detmers et al. 2008; Eldridge et al. 2008), and more recently by Qin et al. (2018) within the context of BBH mergers. Here, we characterize the effects by the timescale, $t_{\rm syn}$, to synchronize the star spin with the orbit (Kushnir et al. 2016)

$$t_{\rm syn} \approx 10\ \mathrm{Myr}\ q^{-1/8}\left(\frac{1+q}{2q}\right)^{31/24}\left(\frac{t_c}{1\ \mathrm{Gyr}}\right)^{17/8}. \quad (4)$$

If fully synchronized with the orbit the spin of the star is aligned and its normalized value is

$$\chi_{\rm syn} \approx 0.5\, q^{1/4}\left(\frac{1+q}{2}\right)^{1/8}\left(\frac{\epsilon}{0.075}\right)\left(\frac{R_2}{2R_\odot}\right)^2 \times\left(\frac{m_2}{30M_\odot}\right)^{-13/8}\left(\frac{t_c}{1\ \mathrm{Gyr}}\right)^{-3/8}, \quad (5)$$

where $\epsilon \equiv I_2/m_2R_2^2$ relates the star's moment of inertia, I_2, to its mass and radius, m_2 and R_2.

Winds. Strong winds that operate at late phases of the stellar evolution lead to angular momentum loss, characterized by $t_w \equiv \chi_*/\dot{\chi}_*$, where χ_* is the star's normalized aligned spin, and $\dot{\chi}_*$ is its angular momentum weighted[6] loss rate. As mentioned earlier, we neglect the winds' impact on the orbital separation and with this the coupling between winds and tidal locking (Qin et al. 2018). Additionally, the larger metallicity of BBHs that form recently (and hence merge with smaller t_c values reflecting smaller initial separations) increases the effects of winds relative to BBHs that formed earlier at larger initial separations. Both effects enhance the winds' impact. These effects will be incorporated within our model by shorter t_w values that will indicate stronger winds.

Initial values. We consider initially synchronized stars $\chi_*(0) = \chi_{\rm syn}$ or nonrotating stars $\chi_*(0) = 0$, denoted by a subscript $_{\rm syn,0}$, respectively. These two extreme initial

[6] Wind from the equatorial plane carries more angular momentum than the average specific angular momentum. If it dominates, angular momentum loss rate is faster than mass-loss rate.

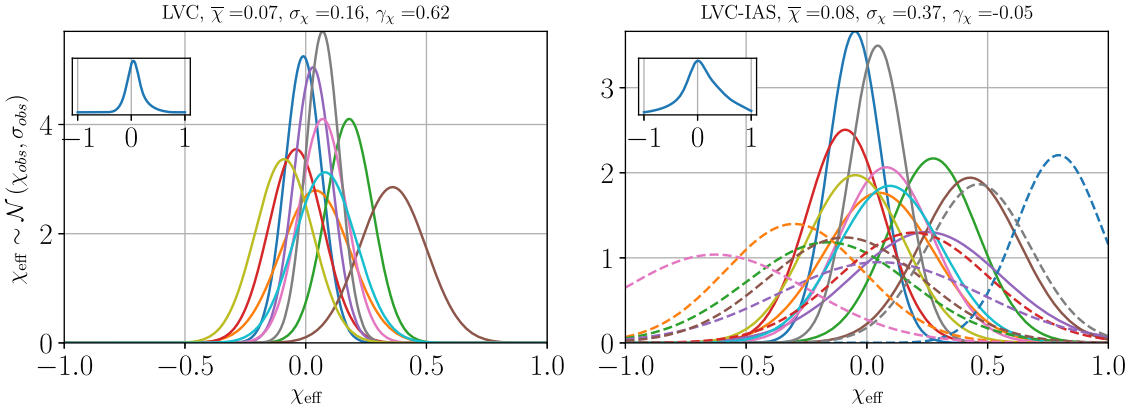

Figure 1. Distribution of the observed $\chi_{\rm eff}$ in the LVC (Left) and IAS (right) data. We approximated each observation as a Gaussian whose mean value and 90% credible interval are the values given in (Abbott et al. 2019b) and (Zackay et al. 2019b), respectively. The inserts show the average distribution. The title indicates the mean $\overline{\chi}$, the standard deviation σ_χ, and the skewness γ_χ.

Table 2
Acceptance Values of Anderson–Darling Test Statistic A^2 for the Different Models

Model	99%	90%	80%	70%	60%	50%	40%	30%	20%	10%	5%	4%	3%	2%	1%
SA_0, SA_{syn}	0.18	0.33	0.44	0.55	0.66	0.8	0.96	1.18	1.49	2.06	2.69	2.88	3.15	3.53	4.19
DA_0, DA_{syn}	0.18	0.33	0.45	0.55	0.67	0.8	0.96	1.18	1.5	2.09	2.71	2.91	3.18	3.55	4.24
$(SA_{0,syn} + DA_{0,syn})/2$	0.18	0.33	0.44	0.55	0.67	0.8	0.96	1.18	1.5	2.08	2.7	2.9	3.17	3.55	4.16
ISO_{low}, ISO_{flat}, ISO_{high}	0.18	0.33	0.44	0.55	0.66	0.79	0.95	1.16	1.47	2.05	2.64	2.85	3.11	3.49	4.12

conditions reflect the large uncertainty in the earlier evolution of the stars.

Evolution. The combined effects of tidal forces and winds on the stellar spin yield (Kushnir et al. 2016; Hotokezaka & Piran 2017)

$$\frac{d\chi_*}{dt} = \frac{(\chi_{\rm syn} - \chi_*)^{8/3}}{t_{\rm syn}(t_c)} - \frac{\chi_*}{t_w}. \quad (6)$$

We evolve χ_* over the lifetime of the star t_* to obtain the final spin $\chi_*(t_*)$ (see Figure 8 in Appendix A). We fix the stellar lifetime at $t_* = 0.3$Myr. Changing this value will merely amount to rescaling the other timescales $t_{\rm syn}$ and t_w. The ratio $\chi_*(t_*)/\chi_{\rm syn}$ depends on $t_w/t_{\rm syn}(t_c)$ and t_w/t_*. While the latter is of order unity, the former varies over a large range, due to the strong dependence of $t_{\rm syn}$ on t_c (see Equation (4)).

Collapse. If $\chi_*(t_*) \leqslant 1$, the entire star implodes to a BH with $\chi_{\rm BH} = \chi_*(t_*)$. If $\chi_*(t_*) > 1$, a fraction of the matter must be ejected carrying the excess angular momentum and $\chi_{\rm BH} \lesssim 1$ (Stark & Piran 1985). Observations of massive ($>10M_\odot$) Galactic BHs X-ray binaries indicate that massive BHs form in situ in a direct implosion and without a kick (Mirabel 2017). Therefore, we disregard here possible natal kicks (see e.g., Mandel 2016; Tauris et al. 2017; Wysocki et al. 2018) that may tilt the spin and randomize it.

Single/double synchronization. In the single-aligned (SA) scenario tidal locking and winds operate only on the secondary (the lighter) star and the resulting effective spin, $\chi_{\rm BH,2}$, is calculated as outlined above (see Appendix A for details). We take $\chi_{\rm BH,1}$ to be distributed as flat isotropic.[7] We also consider a double-aligned (DA) scenario in which tidal locking and winds operate on both stars in a similar manner.

[7] (Piran & Hotokezaka 2018) assumed in this scenario that the primary always has $\chi_{\rm BH,1} = 0$.

Rates and delay distribution. We assume that the BBHs formation rate follows the star formation rate (SFR; Madau & Dickinson 2014) $R_{\rm SFR}(z) \propto (1+z)^{2.7}/\{1 + [(1+z)/2.9]^{5.6}\}$. This is uncertain, as the progenitors are very massive stars, but we have verified (see Appendix B, Figure 10) that our predictions do not depend strongly on the details of the BBH formation rate. In particular, we also consider a formation rate that follows long GRB (LGRBs) that in turn follow a low metallicity population.

The mergers' rate follows the formation rate with a time delay t_c whose probability is assumed to be distributed as $p_{\rm obs}(t_c) \propto t_c^{-1}$ for $t_c > t_{c,\rm min}$. This last parameter, $t_{c,\rm min}$ is one of the critical parameters of the model as t_c determines the separation between the two progenitors just before the second collapse. $t_{c,\rm min}$ corresponds, therefore, to the minimal separation. The separations above this minimal one are equally distributed in the logarithm.

A detailed description of the implementation of the model and the calculation of the resulting probability distribution is given in Appendix A.

4. Data Analysis

To estimate the validity of each model, we use the Anderson & Darling (1952) test. The Anderson–Darling (AD) statistic is model dependent. To allow for a proper comparison, we obtain the significance level, given in Table 2, of each model independently. For a given model, described by a distribution $p(\chi_{\rm eff})$, the significance test is performed as follows: (i) we sample $\mathcal{N} = 18$ noiseless data points from $p(\chi_{\rm eff})$; (ii) we add an error sampled from a centered Gaussian with a standard deviation, $\overline{\sigma}_{\chi_{\rm eff}} = 0.15$ (the average standard deviation in the observed $\chi_{\rm eff}$ estimates, see Table 1) to each data point; (iii) we evaluate the A^2 statistic of the obtained data set; and (iv) repeating this process 10^6 times gives an empirical distribution

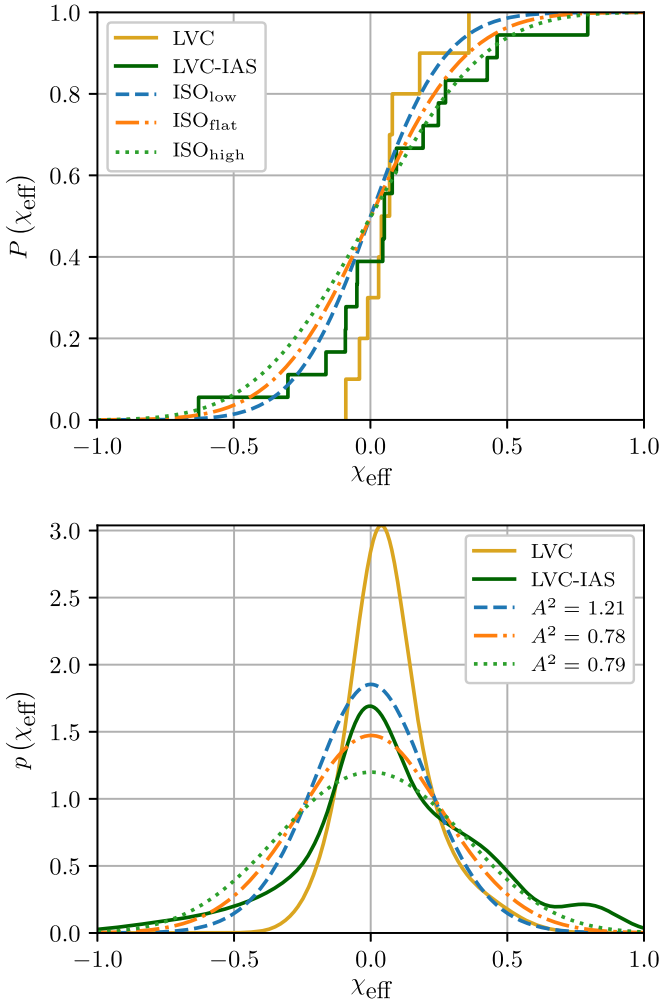

Figure 2. (Top) Comparison of the cumulative distribution, $P(\chi_{\rm eff})$ and (bottom) the probability density function, $p(\chi_{\rm eff})$ of the low, flat, and high isotropic models (with observation errors added) with the LVC–IAS data. The AD statistic, A^2, is marked for each model.

of A^2 from which we obtain the acceptance values (see Table 2).

To test how many events are required to distinguish between two models, we carry out the following procedure. We choose one distributions, denoted $p_{\rm ref}(\chi_{\rm eff})$, as describing the "real world," and compare it with a test distribution, denoted $p_{\rm cmp}(\chi_{\rm eff})$. To do so, we obtain a data set by sampling $\mathcal{N}$ events from $p_{\rm ref}(\chi_{\rm eff})$. We consider those as our "observed" events, and we carry out the same analysis as described earlier to test the compared model against this data set using the AD test. We perform this over a range of sample sizes, $\mathcal{N}$.

Before comparing any model distribution with the data, we must take into account the errors in the estimated $\chi_{\rm eff}$ values. To do so, for each model described by a parameter set λ, we evaluate the theoretical probability, $p_{\rm th}(\chi_{\rm eff};\lambda)$ (see Appendix A for details). We then account for the errors by convolving $p_{\rm th}(\chi_{\rm eff};\lambda)$ with a Gaussian characterized by $\bar{\sigma}_{\chi_{\rm eff}} = 0.15$. The final model prediction is given by

$$p(\chi_{\rm eff};\lambda) = \int_{-1}^{1} p_{\rm th}(\chi'_{\rm eff};\lambda)\frac{e^{-(\chi_{\rm eff}-\chi'_{\rm eff})^2/2\bar{\sigma}^2_{\chi_{\rm eff}}}}{\sqrt{2\pi\bar{\sigma}_{\chi_{\rm eff}}}}d\chi'_{\rm eff}. \quad (7)$$

As some of the events have a lower $p_{\rm astro}$ values we have also analyzed the data taking this probability into account. Each

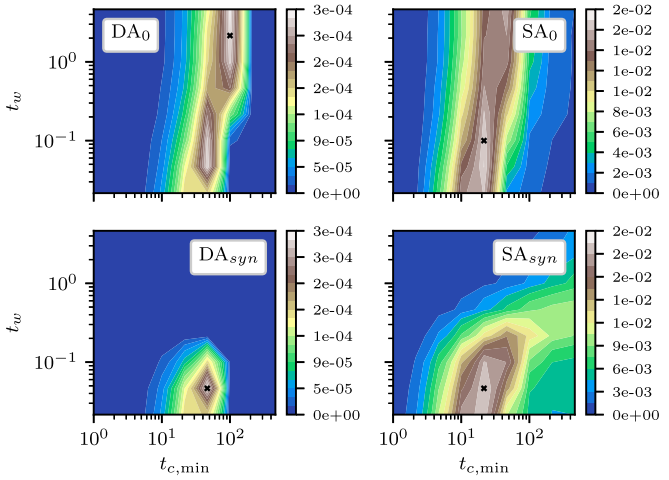

Figure 3. The likelihood $\mathcal{L}$ of the four different field binary models over a range of time parameters, $t_w \in [0.03, 5]$Myr and $t_{c,\rm min} \in [1, 1000]$Myr. The maximum-likelihood values are marked with a $_*$.

one of the events was given a weight that is proportional to its $p_{\rm astro}$. This has a minimal effect on the results (see Figure 2 in Appendix B).

5. Results

We compare the current data with different models in Section 5.1. Given the best model in each category, in Section 5.2 we then address the question of how many events are required to obtain a statistically significant result that will distinguish between the two categories.

5.1. Current Data

We compare the observed LVC–IAS $\chi_{\rm eff}$ distribution with the expected ones for three isotropic distributions: low, flat, and high, (as defined in Farr et al. 2017) and the four field binary models: SA$_{m0,\rm syn}$ and DA$_{m0,\rm syn}$, described above. We optimize the parameters of the field binary models by performing a maximum-likelihood test (see Figure 3).

Isotropic models. Figure 2 depicts a comparison of the distributions of the three isotropic models to the LVC–IAS data. All three isotropic models are acceptable. However, the high model is favored, whereas the low model was the most favorable with the LVC data (Farr et al. 2017).

Field binaries. The models depend on three time parameters, t_*, $t_{c,\rm min}$ and t_w. We take $t_* = 0.3$Myr as the typical[8] lifetime and use the maximum-likelihood (see Figure 3) to determine the best $t_{c,\rm min}$, t_w values. We find good fits (see Figure 4) for all models. The two SA models, initially unsynchronized and synchronized, result in almost identical distributions (using different parameters). Similarly, the two DA models give identical distributions.

SA$_0$ stands out as the preferred model with the highest maximum-likelihood and the most reasonable physical parameters (see Piran & Hotokezaka 2018): $t_{c,\rm min} = \{10 - 100\,{\rm Myr}\}$ (corresponding, for $m_i \approx 30M_\odot$, $q = 1$, to $a = 4 - 7\cdot 10^{11}$ cm) and $t_w = 0.1$–5 Myr, reflecting a wide range of wind timescales. These values, which are on the lower side and correspond to a rather strong winds, reflect

[8] Variation of t_* will amount to scaling of the two other timescales (see Appendix A, Figure 8).

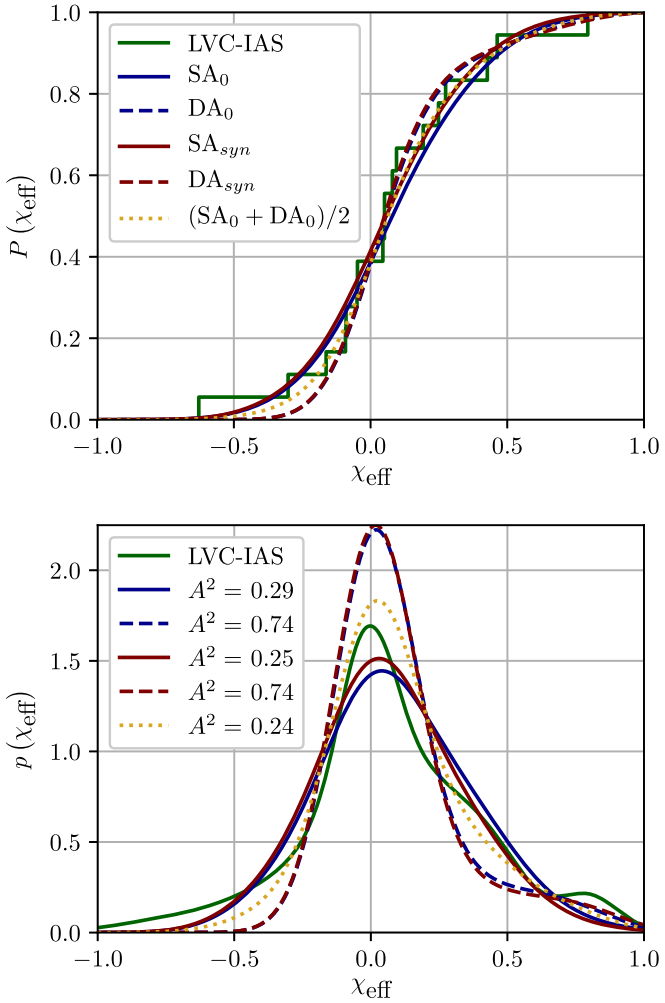

Figure 4. (Top) Cumulative distribution, $P(\chi_{\rm eff})$ and (bottom) the probability density function, $p(\chi_{\rm eff})$ for the LVC–IAS data and different field binary models (using the best fitted parameters ($t_{c,\rm min}$, t_w)Myr: SA$_0$: (20, 0.1), DA$_0$: (100, 1), SA$_{\rm syn}$: (20, 0.05), DA$_{\rm syn}$: (50, 0.05), and a mixed model, (SA$_0$ + DA$_0$)/2, taken with SA$_0$ parameters). Note the excess of intermediate and high positive $\chi_{\rm eff}$ in these models.

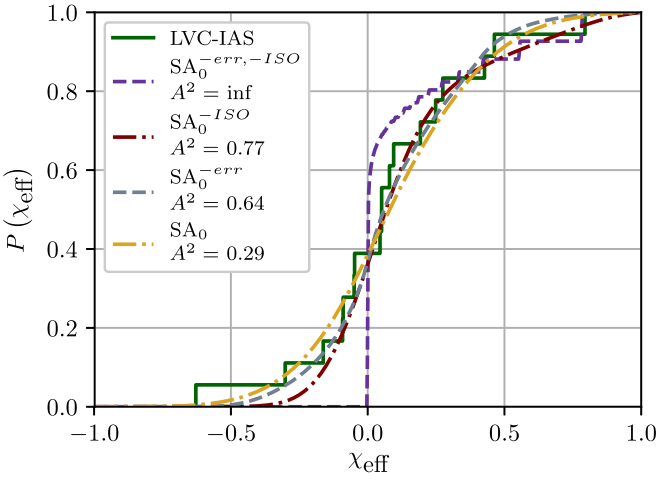

Figure 5. Same as Figure 4, but comparing different SA$_0$ models. The curve (superscript -err,-*ISO*) corresponds to one of the models in Piran & Hotokezaka (2018) that arise when measurements errors and an isotropic spin component for the primary BH are not taken into account. Clearly, such a model has no negative $\chi_{\rm eff}$ values.

probably the fact that our model underestimates somewhat the effect of winds. The maximum-likelihood of SA$_{\rm syn}$ is comparable with the one of SA$_0$, but the former requires somewhat stronger winds ($t_w < 0.1$Myr) and is valid at a more confined range. SA$_0$ and DA$_0$ have a comparable broad range of allowed physically acceptable parameters, but the latter has a smaller maximal likelihood. The DA$_{\rm syn}$ model has the smallest feasible parameter phase space and seems least likely. We also consider, as an example, a model that combines the two with 0.5 (SA$_0$ + DA$_0$) using the best-fit parameters of the SA$_0$ model. Even without optimizing the relative ratio of the two cases and the model parameters, this model fits the data slightly better than all others. When considering different stellar models, the numerical factors that appear in Equations (4) and (5), as well as the typical stellar lifetime, t_*, vary. However, variations in these factors will only amount to a variations in the best-fit parameters, and not to the quality or the overall behavior of the different scenarios.

Figure 5 depicts different SA$_0$ models demonstrating the effect of the errors on the model, as well as the contribution of the addition of an isotropic spin χ_1 into the SA scenario. Both influence the resulting $\chi_{\rm eff}$ distributions giving a non-zero probability to $\chi_{\rm eff} > 0.5$ and to $\chi_{\rm eff} < 0$ events.[9]

5.2. Future Estimates

As stated earlier, the current data set is insufficient. Even the least preferred model, the low-isotropic, is consistent at ∼20% with the data. We turn now to address the following question: Assuming that one of the models is the correct one, how many mergers are needed to rule out the others? To do so, we choose one of the models as the fiducial one, characterized by a distribution $p_{\rm ref}(\chi_{\rm eff})$. We can now test any model, denoting it is probability density as $p_{\rm cmp}(\chi_{\rm eff})$, against the reference model. To do so, we carry out the following procedure: (i) for each sample size, $\mathcal{N}$, we create an AD acceptance table for $p_{\rm cmp}(\chi_{\rm eff})$; (ii) we sample 10^5 different data sets (numerical tests reveal that this number is sufficient) of size $\mathcal{N}$ from $p_{\rm ref}(\chi_{\rm eff})$; and (iii) we compute the average acceptance percentage of these data sets. We repeat this procedure for $\mathcal{N}$ values ranging from 20 to a few hundred choosing different models as the fiducial one and as the tested ones.

Within the "field evolution" models, we consider the SA$_0$ model and the DA$_0$ with the best-fit parameters over the current data set. We compare those with the three isotropic models: low, flat, and high. We also consider a mixed model in which 50% of the event are SA$_0$ field evolution binaries, while the other 50% are flat isotropic.

Figure 6 (top) depicts the resulting acceptance (1-rejection) probability of different tested models. It appears that 50–100 (150–250) mergers are require to distinguish the SA$_0$ model from the isotropic ones at the 5% (1%) confidence level. The DA$_0$ model includes more positive high-spin events and fewer negative-spin ones. Hence, as expected, it is easier to distinguish it from the isotropic models. As shown in Figure 6 (bottom), 30–60 (50–120) mergers are sufficient to distinguish between the DA$_0$ model and the different isotropic models at the 5% (1%) confidence level. A caveat in the above estimate is that it cannot account for possible variations in the

[9] Natal kicks, which we have neglected, can also give rise to negative $\chi_{\rm eff}$ values (Wysocki et al. 2018).

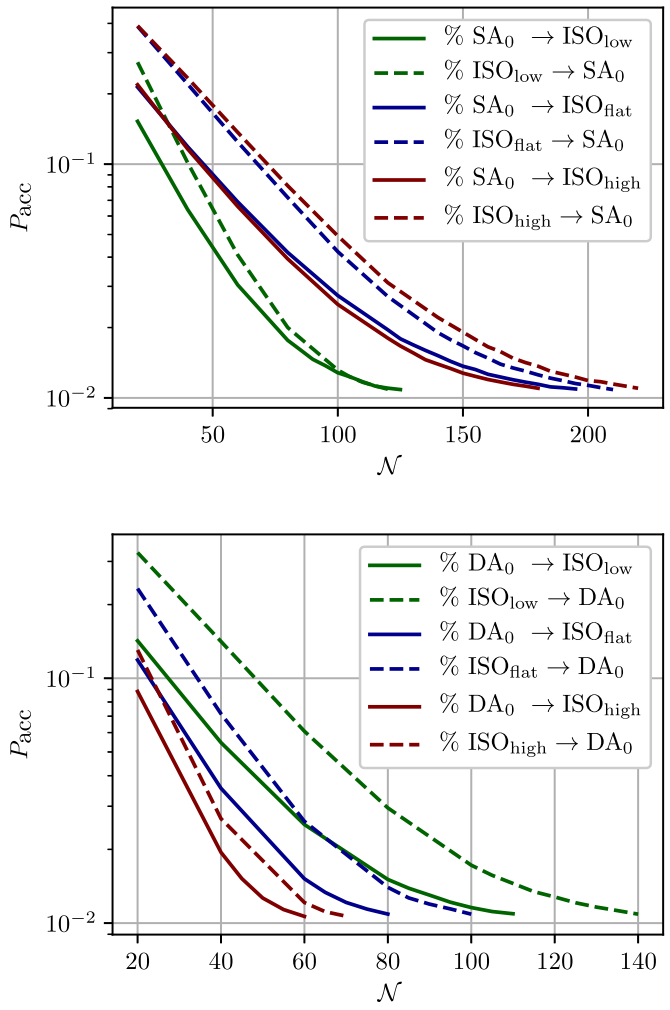

Figure 6. Probability of acceptance, P_{acc}, (or rejection that is 1–P_{acc}) level of different models as a function of the number $\mathcal{N}$ of events detected. We compare the field evolution models, SA_0 (top) and DA_0 (bottom), with the three isotropic models, low flat, and high. Solid curves assume that the field evolution model describes the "real world," and depict the acceptance significance of the isotropic models. Dashed curves assume that the isotropic models are the correct one and estimate the acceptance level for the respective field model. As expected, it is easier to distinguish between the low-isotropic and the SA_0 model than to distinguish between the flat and high isotropic models and SA_0. Furthermore, a fewer events are needed (as compared with SA_0) to distinguish between the DA_0 field evolution model and the isotropic models.

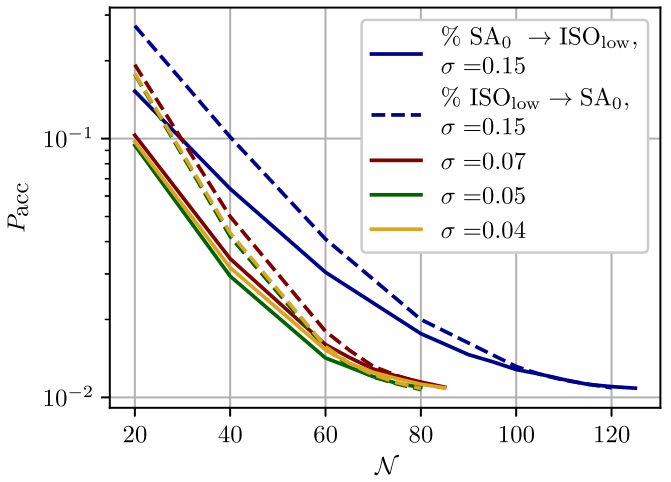

Figure 7. Acceptance probability as a function of the number of mergers (same as Figure 6) between the SA_0 and the low-isotropic models. Solid lines test the acceptance of a low-isotropic model assuming that the correct model is SA_0. Dashed lines consider the opposite. The standard deviation in measuring χ_{eff} varies from 0.15 as in the current observed sample to 0.04.

best-fit parameters of the field binaries models SA_0, DA_0 that may arise in a large data set. The situation is more complicated when we consider mixed models that combine both field binaries and capture. A few hundred mergers are needed to distinguish between these models and "pure" field binaries or "pure" capture models.

One may wonder whether a few strong events whose χ_{eff} can be determined at a higher accuracy can change these conclusions. To check this, we carried out the same test using now different values of $\bar{\sigma}_{\chi_{eff}}$, the standard deviation in the estimation of χ_{eff} (see Figure 7). As expected, fewer events would suffice with a lower $\bar{\sigma}_{\chi_{eff}}$. If $\bar{\sigma}_{\chi_{eff}}$ is a quarter of its current value 25–50 (80–120), events are needed to distinguish at the 5% (1%) confidence level between the SA_0 model and the isotropic ones.

6. Conclusions

The observed low effective spins, which were centered around 0, in the LVC O1–O2 sample favored low-spin isotropic distributions (Farr et al. 2017), and hence capture scenarios. We have shown here that while the combined LVC–IAS data set, which includes a high χ_{eff} binary, cannot rule out any model it favors field binaries over capture.

Within the field binary models, the high χ_{eff} merger implies a significant fraction of short ($t_c \sim 20$Myr) mergers, namely BBHs that at formation had small, but reasonable (4–7 $\times$ 10^{11}cm), separations. Overall, the LVC–IAS sample brackets nicely the phase space of the field binary model with 10Myr $\lesssim t_{c,\min} \lesssim$ 100Myr, 0.05Myr $\lesssim t_w \lesssim$ 5Myr.

While the isotropic scenario is disfavored, it is not ruled out. Among those models the high variant becomes the most favorable and the low the least. It is interesting to note that recently Romero-Shaw et al. (2019) have shown that the eccentricity of all the events in the LVC sample are smaller than 0.02 to 0.05, whereas a capture scenario suggests that 5% of the events should have larger eccentricity. Again, while this result does not rule out the capture scenarios they support our findings. Clearly, a mixture of field binaries and capture is possible. In this case, we expect that the former will be dominant. However, given the limited data, we did not explore this possibility here. Considering future observations, we note that the hallmark of the field binaries scenario is a preferably positive χ_{eff} distribution with a few large positive χ_{eff} mergers. At the same time, unless kicks are very significant and dominate the BHs spin distribution, large negative χ_{eff} will pose a problem for the field binary model. We have shown that for the models considered here, we will need 30–250 events, depending on the details of the model and the level of confidence required to distinguish between the two scenarios. Higher signal-to-noise ratio data that has a better determined χ_{eff} value would require a fewer events. Hundreds of events will be needed to determine the ratio of capture to field evolution events in mixed model that includes both capture and field binaries, or to distinguish those from pure capture or pure field evolution models.

We thank Tejaswi Venumadhav, Barak Zackay, Javier Roulet, Liang Dai, and Matias Zaldarriaga for sharing their data with us prior to publication, and we acknowledge fruitful discussions with Ofek Birnholtz, Giacomo Fragione, Kenta Hotokezaka, Ehud Nakar, Bill Press, Nicholas C. Stone, and Barak Zackay. The research was supported by an advanced ERC grant (TReX), by the I-Core center of excellence of the CHE-ISF (TP) and by the Israeli Council for Higher Education (ZP).

Appendix A
The Model Distribution for Field Binaries

The model distribution, $p_{th}(\chi_{\rm eff};\,\lambda)$, $\lambda=\{{\rm SA}_{0,{\rm syn}}/{\rm DA}_{m0,syn},\,m_1,\,m_2,\,t_{c,\min},\,t_w,\,t_*\}$, is derived under the assumptions given in the main text.

We take the BBH formation rate per volume element per unit comoving time, $R(z)$, to follow the SFR (we also consider other rates; see Appendix B).

The mergers' rate follows the formation rate with a delay t_c whose probability is assumed to be $p_{obs}(t_c)\propto t_c^{-1}$ for $t_c>t_{c,\min}$. This allows us to define the probability that the merger occurred at redshift z_c as

$$p(z_c)=\frac{1}{t_c(z_c)}\frac{R(z_c)}{1+z_c}\frac{d{\rm t_c}}{dz_c}. \tag{8}$$

We approximate, implicitly, that all mergers take place now (relaxing this assumption and assuming that the mergers take place between $z=0$ and $z=0.5$ does not change our results).

For a given t_c and fixed t_w, t_*, we compute the final stellar spin, $\chi_*(t_*)$ by integrating (Equation (6) of the main text)

$$\frac{d\chi_*}{dt}=\frac{(\chi_{\rm syn}-\chi_*)^{8/3}}{t_{\rm syn}(t_c)}-\frac{\chi_*}{t_w}, \tag{9}$$

from 0 to t_*. As initial conditions, we take

$$\chi_*(0)=\begin{cases}0 & \text{unsynchronized,}\\ \chi_{\rm syn} & \text{synchronized.}\end{cases} \tag{10}$$

Figure 8 depicts the results of this integration in terms of $\chi_*/\chi_{\rm syn}$, as a function of t/t_w for different ratios of $\tilde{t}_{\rm syn}\equiv\chi_{\rm syn}^{-5/3}(t_{\rm syn}/t_w)$.

The BH spin after the collapse is then given by

$$\chi_{\rm BH}=\min\{\chi_*(t_*),\,1\}. \tag{11}$$

Under the assumption that $\chi_{\rm BH}$ is deterministic with regard to its parameters, we may write it is distribution using the chain rule,

$$p(\chi_{\rm BH};\,\lambda)=\frac{1}{t_c(z_c)}\frac{R(z_c)}{1+z_c}\frac{d\chi_{\rm BH}}{d{\rm t_c}}\frac{d{\rm t_c}}{dz_c}, \tag{12}$$

where we calculate numerically the derivative $d\chi_{\rm BH}/d{\rm t_c}$, following the integration of Equation (6) above.

To obtain the final $\chi_{\rm eff}$ distribution,

$$\chi_{\rm eff}=\frac{\chi_{\rm BH,1}+q\chi_{\rm BH,2}}{(1+q)}, \tag{13}$$

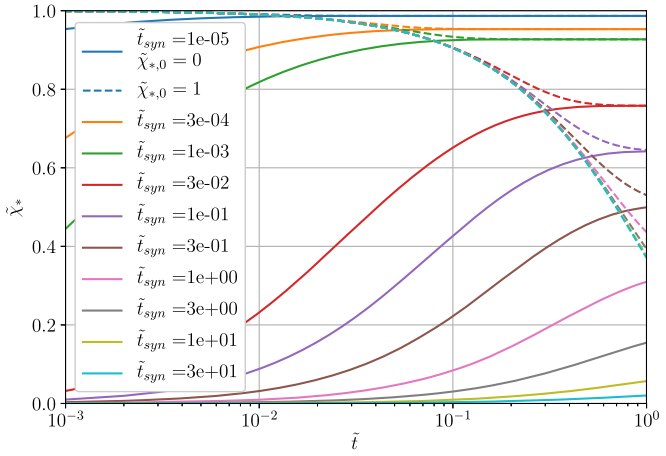

Figure 8. $\tilde{\chi}\equiv\chi_*/\chi syn$ as a function of $\tilde{t}\equiv t/t_w$ for different values of $\tilde{t}_{\rm syn}\equiv\chi_{\rm syn}^{-5/3}(t_{\rm syn}/t_w)$.

we consider the different scenarios separately.

1. *SA.* $\chi_{\rm BH,1}$ is distributed as *flat* isotropic and $\chi_{\rm BH,2}$ is given by Equation (12). To find the resulting distribution of $\chi_{\rm eff}$ we sample each (from the respective distribution) and calculate the empirical distribution of their weighted sum.
2. *DA.* Using the above procedure, for a given t_c,we calculate $\chi_{\rm BH,1}$ and $\chi_{\rm BH,2}$. Using the numerical values of the derivative, $d\chi_{\rm eff}/d{\rm t_c}$, we obtain the distribution

$$p(\chi_{\rm eff};\,\lambda)=\frac{1}{t_c(z_c)}\frac{R(z_c)}{1+z_c}\frac{d\chi_{\rm eff}}{d{\rm t_c}}\frac{d{\rm t_c}}{dz_c}. \tag{14}$$

Appendix B
Additional Tests

The mass distribution. The masses used in the estimates are the average values of the sample, $\overline{m}_1=38M_\odot$ and $\overline{m}_2=24M_\odot$. To explore the effect of the different masses, we also use the masses of the observed events and sample over the mass distribution. The results are shown in Figure 9 for the SA distribution and for the isotropic models whose $\chi_{\rm eff}$ distribution is affected (becomes broader) when mass ratio is taken into account. We find that the results are almost the same as those obtained using the average mass and mass ratio.

The event rate. We use the SFR as the event rate for the formation of BBH. We also consider the possibility that BBH follow the LGRB rate, as it was suggested that long GRBs indicate the formation of a BBH (Piran & Hotokezaka 2018), and a (ad hoc) constant formation rate. Figure 10 demonstrates that the resulting distribution is practically independent of the assumption on the SFR.

p_{astro} weight. The observed events are given a probability that the event is of astrophysical, $p_{\rm astro}$. Weighting the events using this value to obtain the observed distribution does not affect the goodness of fit (A^2 score) of our models; see Figure 11.

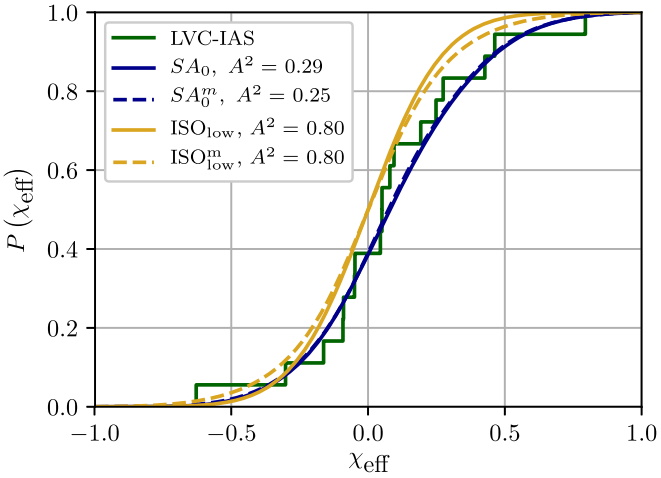

Figure 9. Models evaluated using a mixture of mass ratios, m_1, m_2. That is, for each model we find it is prediction to each of the $N = 18$ observed masses and consider the average of this predictions as the final probability of the model. We denote the mixture probabilities a superscript m.

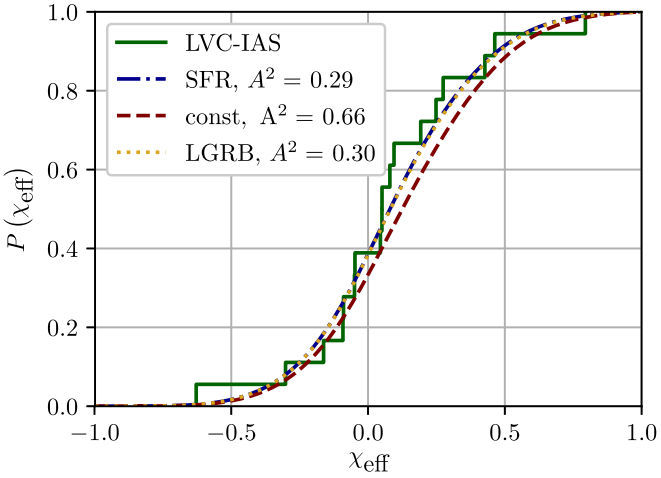

Figure 10. Effect of the rate function, $R(z)$ on the model prediction. All rates are evaluated under the $\mathrm{SA_0}$ scenario.

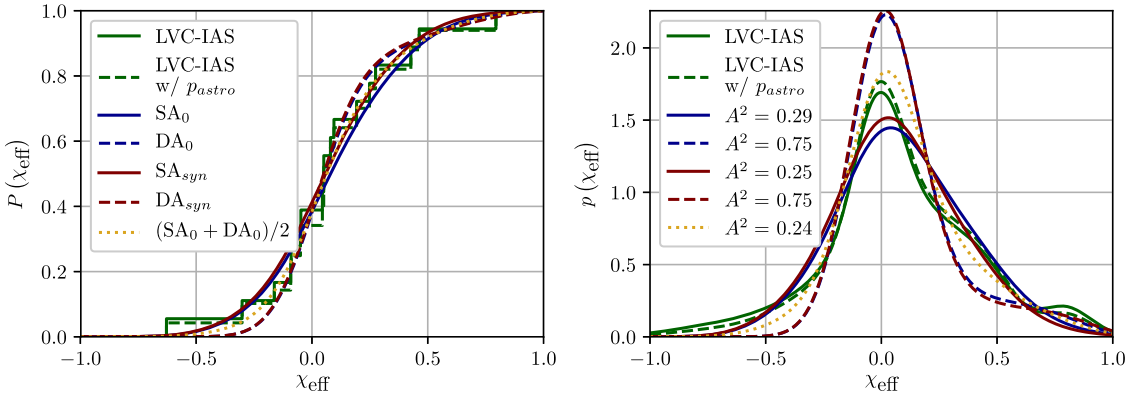

Figure 11. Effect of weighting the observed events by p_{astro} on the obtained observed distribution and goodness of fit to the models (calculated with the same parameters).

References

Abbott, B. P., Abbott, R., Abbott, T. D., et al. 2016, PhRvL, 116, 061102
Abbott, B. P., Abbott, R., Abbott, T. D., et al. 2019a, ApJL, 882, L24
Abbott, B. P., Abbott, R., Abbott, T. D., et al. 2019b, PhRvX, 9, 031040
Anderson, T. W., & Darling, D. A. 1952, Ann. Math. Statist, 23, 193
Antonini, F., & Rasio, F. A. 2016, ApJ, 831, 187
Bartos, I., Kocsis, B., Haiman, Z., & Márka, S. 2017, ApJ, 835, 165
Bavera, S. S., Fragos, T., Qin, Y., et al. 2020, A&A, 635, 97
Belczynski, K., Holz, D. E., Bulik, T., & O'Shaughnessy, R. 2016, Natur, 534, 512
Belczynski, K., Klencki, J., Fields, C. E., et al. 2017, arXiv:1706.07053
Bird, S., Cholis, I., Muñoz, J. B., et al. 2016, PhRvL, 116, 201301
Blinnikov, S., Dolgov, A., Porayko, N. K., & Postnov, K. 2016, JCAP, 11, 036
Brown, G. E., Lee, C. H., Wijers, R. A. M. J., Lee, H. K., Israelian, G., & Bethe, H. A. 2000, NewA, 5, 191

Campanelli, M., Lousto, C. O., Marronetti, P., & Zlochower, Y. 2006a, PhRvL, 96, 111101
Campanelli, M., Lousto, C. O., & Zlochower, Y. 2006b, PhRvD, 74, 041501
Cantiello, M., Yoon, S. C., Langer, N., & Livio, M. 2007, A&A, 465, L29
Detmers, R. G., Langer, N., Podsiadlowski, P., & Izzard, R. G. 2008, A&A, 484, 831
Eldridge, J. J., Izzard, R. G., & Tout, C. A. 2008, MNRAS, 384, 1109
Farr, W. M., Stevenson, S., Miller, M. C., et al. 2017, Natur, 548, 426
Fragione, G., Grishin, E., Leigh, N. W. C., Perets, H. B., & Perna, R. 2019, MNRAS, 488, 47
Fragione, G., & Kocsis, B. 2018, PhRvL, 121, 161103
Hoang, B.-M., Naoz, S., Kocsis, B., Rasio, F. A., & Dosopoulou, F. 2018, ApJ, 856, 140
Hotokezaka, K., & Piran, T. 2017, ApJ, 842, 111
Ioka, K., Chiba, T., Tanaka, T., & Nakamura, T. 1998, PhRvD, 58, 063003
Ivanova, N., Justham, S., Chen, X., et al. 2013, A&ARv, 21, 59
Izzard, R. G., Ramirez-Ruiz, E., & Tout, C. A. 2004, MNRAS, 348, 1215
Kashlinsky, A. 2016, ApJL, 823, L25
Kocsis, B., & Levin, J. 2012, PhRvD, 85, 123005
Kushnir, D., Zaldarriaga, M., Kollmeier, J. A., & Waldman, R. 2016, MNRAS, 462, 844
Madau, P., & Dickinson, M. 2014, ARA&A, 52, 415
Mandel, I. 2016, MNRAS, 456, 578
Mandel, I., & de Mink, S. E. 2016, MNRAS, 458, 2634
Mandel, I., & O'Shaughnessy, R. 2010, CQGra, 27, 114007
Marchant, P., Langer, N., Podsiadlowski, P., Tauris, T. M., & Moriya, T. J. 2016, A&A, 588, A50
McKernan, B., Ford, K. E., Saavik, B. J., et al. 2018, ApJ, 866, 66
Miller, M. C., & Lauburg, V. M. 2009, ApJ, 692, 917
Mirabel, I. F. 2017, in IAU Symp. 324, New Frontiers in Black Hole Astrophysics, ed. A. Gomboc (Cambridge: Cambridge Univ. Press), 303
O'Leary, R. M., Kocsis, B., & Loeb, A. 2009, MNRAS, 395, 2127
O'Leary, R. M., Meiron, Y., & Kocsis, B. 2016, ApJL, 824, l12
O'Shaughnessy, R., Gerosa, D., & Wysocki, D. 2017, PhRvL, 119, 011101
Petrovic, J., Langer, N., & van der Hucht, K. A. 2005, A&A, 435, 1013
Phinney, E. S. 1991, ApJL, 380, L17
Piran, T., & Hotokezaka, K. 2018, arXiv:1807.01336
Portegies Zwart, S. F., & McMillan, S. L. W. 2000, ApJL, 528, L17
Postnov, K. A., & Mitichkin, N. A. 2019, JCAP, 2019, 044
Qin, Y., Fragos, T., Meynet, G., et al. 2018, A&A, 616, A28
Rodriguez, C. L., Amaro-Seoane, P., Chatterjee, S., et al. 2018, PhRvD, 98, 123005
Rodriguez, C. L., Zevin, M., Pankow, C., Kalogera, V., & Rasio, F. A. 2016, ApJL, 832, L2
Romero-Shaw, I. M., Lasky, P. D., & Thrane, E. 2019, MNRAS, 490, 5210
Roulet, J., & Zaldarriaga, M. 2019, MNRAS, 484, 4216
Rubin, S. G., Sakharov, A. S., & Khlopov, M. Yu. 2001, JETP, 92, 921
Sasaki, M., Suyama, T., Tanaka, T., & Yokoyama, S. 2016, PhRvL, 117, 061101
Secunda, A., Bellovary, J., Mac Low, M.-M., et al. 2019, ApJ, 878, 85
Sigurdsson, S., & Hernquist, L. 1993, Natur, 364, 423
Stark, R. F., & Piran, T. 1985, PhRvL, 55, 891
Stevenson, S., Vigna-Gómez, A., Mandel, I., et al. 2017, NatCo, 8, 14906
Stone, N. C., Metzger, B. D., & Haiman, Z. 2017, MNRAS, 464, 946
Tauris, T. M., Kramer, M., Freire, P. C. C., et al. 2017, ApJ, 846, 170
Tutukov, A. V., & Yungelson, L. R. 1993, MNRAS, 260, 675
van den Heuvel, E. P. J. 2007, in AIP Conf. Ser. 924, The Multicolored Landscape of Compact Objects and Their Explosive Origins, ed. T. di Salvo et al. (Melville, NY: AIP), 598
Venumadhav, T., Zackay, B., Roulet, J., Dai, L., & Zaldarriaga, M. 2019a, arXiv:1904.07214
Venumadhav, T., Zackay, B., Roulet, J., Dai, L., & Zaldarriaga, M. 2019b, PhRvD, 100, 023011
Wiktorowicz, G., Wyrzykowski, Ł., Chruslinska, M., et al. 2019, ApJ, 885, 1
Wysocki, D., Gerosa, D., O'Shaughnessy, R., et al. 2018, PhRvD, 97, 043014
Zackay, B., Dai, L., Venumadhav, T., Roulet, J., & Zaldarriaga, M. 2019a, arXiv:1910.09528
Zackay, B., Venumadhav, T., Dai, L., Roulet, J., & Zaldarriaga, M. 2019b, PhRvD, 100, 023007